Establishment and parameter calibration of the discrete element model for typical clay in hilly and mountainous areas

Fei Chen[1,2], Li Yang[1,2], Tao Cui[1,2], Dongxing Zhang[1,2], Xiantao He[1,2], Kailiang Zhang[1,2*]

(1. *College of Engineering, China Agricultural University, Beijing 100083, China*;
2. *The Key Laboratory of Soil-Machine-Plant System, Ministry of Agriculture and Rural Affairs, Beijing 100083, China*)

Abstract: The mechanism of the interaction between the furrow opener and clay is the basis for optimizing the performance of the furrow opener. However, there is currently a lack of discrete element simulation parameters that can accurately simulate the actual furrowing operation. This paper considers the combined influence of clay particle bonding and adhesion-wetness based on the Hertz-Mindlin with Bonding V2 (Bonding V2) and Hertz-Mindlin with JKR V2 (JKR V2) contact models. The contact parameters of the JKR V2 contact model between clay particles and between clay and the furrow opener were obtained through simulations and physical tests of the clay angle of repose (AOR), static friction between clay and the furrow opener, and rolling friction. The test results show that the normal/tangential stiffness per unit area has a greater impact on the simulation results of the clay compaction. The bonding parameters of the Bonding V2 contact model were determined by screening significant factors through Plackett-Burman (PB) tests, narrowing the range of significant parameters through steepest climb tests, and optimizing parameters through Box-Behnken Design (BBD) tests. Based on the results of the above tests, the accuracy of the Bonding V2 and JKR V2 contact models and the improvement over a single model were verified through direct shear soil simulation and physical tests. Based on the Bonding V2 and JKR V2 contact models and the multibody dynamics model of the furrow opener, the coupling simulation parameters of the seeder furrow operation were optimized to obtain the optimal furrow opening operation parameters under uphill and downhill conditions. Field tests further verified the simulation realism and feasibility of the Bonding V2 and JKR V2 contact models. The Bonding V2 and JKR V2 contact models for clay in hilly and mountainous areas (HAMA) can provide a reference for modeling clay in HAMA and simulating the contact between the furrow opener and other contact parts during the furrow opener operation.

Keywords: DEM, Bonding V2 contact model, JKR V2 contact model, hilly and mountainous areas, clay, furrow opening, Parameter calibration

DOI: 10.25165/j.ijabe.20251805.9794

Citation: Chen F, Yang L, Cui T, Zhang D X, He X T, Zhang K L. Establishment and parameter calibration of the discrete element model for typical clay in hilly and mountainous areas. Int J Agric & Biol Eng, 2025; 18(5): 26–38.

1 Introduction

The sown area of crops in China's HAMA accounts for one-third of the nation's total area, and in 11 provinces (municipalities, autonomous regions) nationwide, the ratio of HAMA to arable land area exceeds 60%. The surface slope of HAMA varies greatly, with cultivated land ranging from 0° to 15°, accounting for 87.5%. The cultivated land at 15°-25° and above 25° accounts for 9.2% and 3.3%, respectively[1]. However, the level of mechanization in these areas is significantly lower than the national average. The complex and varied terrain complicates the operation of seeders, and the complex soil characteristics (wet, sticky, aggregative, and adhesive) further challenge the normal operation of these machines[2]. Therefore, optimization research on furrow opening operations of seeding machines in HAMA first needs to explore the interaction dynamics between the clay and the furrow opening devices in HAMA. Solely relying on field tests, limitations due to seasonal restrictions and the difficulty in uncovering the micro-level movement characteristics of soil particles are encountered. Currently, most studies combine discrete element numerical simulation with test approaches. With the continuous enhancement of computer performance, utilizing numerical simulation to assist in the study of mechanical properties has become the current trend. For typical granular materials like soil, the Discrete Element Method (DEM) is generally employed in simulation modeling and parameter calibration[3].

Due to the difficulty in practically measuring the modeling, simulation, motion, and force processes of discontinuous granular materials such as soil, seeds, and corn, the DEM has become the mainstream research method. By treating soil and other granular materials as aggregates of numerous discrete, independently moving particles, DEM can intuitively reflect the forces, displacements, and other properties experienced by each particle[4,5]. Currently, domestic and international experts and scholars are using the DEM to conduct in-depth research on establishing effective DEM models for various types of soil, as well as the motion and force patterns of soil particles under the influence of soil-engaging components. In terms of soil parameter calibration, Mudarisov et al.[6] evaluated the role of contact model parameters in wet soil modeling using the discrete element method. Yang et al.[7] used the soil AOR and direct shear

Received date: 2025-03-19 **Accepted date:** 2025-07-10

Biographies: Fei Chen, PhD candidate, research interest: precision agriculture, Email: b20223070613@cau.edu.cn; **Li Yang**, PhD, Professor, research interest: precision agriculture, Email: yangli@cau.edu.cn; **Tao Cui**, PhD, Associate Professor, research interest: full mechanization of corn production, Email: cuitao@cau.edu.cn; **Dongxing Zhang**, PhD, Professor, research interest: full mechanization of corn production, Email: zhangdx@cau.edu.cn; **Xiantao He**, PhD, Associate Professor, research interest: research interest: precision agriculture, Email: hxt@cau.edu.cn.

***Corresponding author: Kailiang Zhang**, PhD, Associate Professor, research interest: strawberry harvesting robot. College of Engineering, China Agricultural University, No.17 Qinghua East Road, Haidian District, Beijing 100083, China. Tel: +86-10-62737765, Email: zhang_kailiang@cau.edu.cn.

characteristics to determine important discrete element parameters for vineyard soil in the northwest region of China. Yang et al.[8] measured the particle contact model parameters for soil with specific moisture content in the southwest region. Aikins et al.[9] calibrated the hysteretic spring contact model for Australian clay and validated it in practical operations. Zhou et al.[10] calibrated bonding model parameters for two typical soils in corn planting fields. In terms of the motion and force patterns of soil and soil-engaging components, Li et al.[11] determined the contact model parameters for two moisture contents of sticky black soil and two materials of soil-contacting components. Lu et al.[12] established and validated a discrete element model of the interaction mechanism between soil, seeds, and covering devices within seed furrows. Sun et al.[13] calibrated the simulation parameters of the interaction contact model between soil and rotary tillage components in the sloped land of the Loess Plateau. Yang et al.[14] calibrated discrete element parameters to explore the interaction mechanisms between layered frost-resistant soil and contact-type soil-cleaning machines in the northwest region. In the above studies, only a single discrete element contact model was used to simulate soil properties. Although a single Bond model can simulate the discontinuity and aggregation of clay, in the interaction between the trenching component and the clay, the cohesive bonds between clay particles were used to simulate the aggregation effect of the soil. The cohesive bonds broke after being impacted by the furrow opening component and could not be regenerated, which is consistent with the mechanical behavior of clay becoming loose after furrow opening[10,15,16]. However, it cannot effectively simulate the adhesive properties formed by the influence of high moisture content on clay. The JKR model is a cohesive contact model that can simulate wet cohesive particles[8,17-19]. Additionally, many studies have already combined the Bond model and JKR model to jointly simulate the properties of clay or other materials [16,20-23].

Therefore, in order to accurately simulate the wet adhesion, agglomeration, and discontinuous characteristics of the clay in HAMA, the Bonding V2 and JKR V2 contact models are added between the clay and clay to simulate the compaction and adhesion of the clay in HAMA, and the JKR V2 contact model is added between the clay and furrow opener to simulate the adhesion between the clay and furrow opener. This provides a simulation of the furrow operation of the planter in HAMA that is closer to reality.

Therefore, based on the above analysis, in order to solve the problems in the existing research, the content and main innovations of this study are as follows:

(1) The JKR V2 and Bonding V2 contact models were used to simulate the wet adhesion, agglomeration, and discontinuous characteristics of clay.

(2) Physical and simulation tests of the AOR, static friction, and rolling friction were carried out for the operational mechanism of clay-clay and clay-65Mn and the calibration of the contact parameters of the JKR V2 contact model. PB tests, steepest ascent tests, and BBD tests based on the clay compaction as the response value were designed for the calibration and optimization of the adhesion parameters of the Bonding V2 contact model.

(3) The actual accuracy of the contact parameters of the JKR V2 contact model and the bonding parameters of the Bonding V2 bonding model were verified using physical and simulation tests of direct shear of clay, simulation of furrow operation, and field tests.

This study can provide more reliable contact parameters for the JKR V2 contact model and adhesion parameters for the Bonding V2 adhesion model for accurately simulating the operation of a planter in HAMA under natural conditions using the discrete element method. This can accurately simulate the characteristics of clay in HAMA and provide important support for the research and development of special planters for HAMA.

2 Materials and methods

2.1 Measurement of test parameters and determination of discrete element model

2.1.1 Measurement of test parameters

Typical clay samples from the HAMA were collected in May 2024 from the sowing farmland in Jinbi Town, Qianxi City, Guizhou Province (105.94°N, 26.96°E). According to actual measurements using a slope inclinometer (pro360, accuracy 1°, Fengshang Hardware), the slope of the farmland is 15°. Figures 1a and 1b show the clay sampling process. A ring cutter with a volume of 2×10^{-4} m^3 (200 cm^3, inner diameter 70 mm×height 52 mm) is used to collect the 0-10 cm topsoil clay layer, and Vaseline is applied evenly on the inner wall of the ring cutter, with the edge of the ring cutter perpendicular to the clay. The handle is placed above the ring knife and pressed firmly to make the ring cutter cut into the clay. When the ring cutter is slightly lower than the clay level, the soil around the ring cutter is removed. Then, the ring knife is gently removed, excess clay is scraped off, and the soil at both ends of the ring cutter is made flat to complete the collection, along with loose clay for subsequent AOR determination. The clay moisture content was tested in compliance with ISO 662:2016 standards, using a constant temperature drying oven (1 010 008, power 0.8 kW, Shaoxing Shangcheng Instrument Manufacturing Co., Ltd.), which measured the clay moisture content to be 22.46%±1%. A standard volume container (500 mL, inner diameter 75 mm×height 115 mm) and an electronic balance (capacity 500 g, accuracy 0.01 g, JA5003A, Shanghai Jingtian Electronic Instrument Co., Ltd.) were used to measure the clay density, with the average value of 1689 kg/m^3 used as the final simulation parameter.

a. Slope measurement b. Clay sampling using a ring knife c. Clay sieving

Figure 1 Clay sampling

Clay samples from various sampling points were weighed using an electronic scale (Model LQ-C10002, d=0.01 g, manufactured by Kunshan Youkewei Electronic Technology Co., Ltd.) at 500 g each. The samples were then sieved using an electric sieve shaker (manufactured by Shangyu Huafeng Hardware Instrument Co., Ltd., Shaoxing City) and standard test sieves (Figure 1c), resulting in soil

particle size distributions of >5 mm, 1-5 mm, and <1 mm, with respective proportions of 24.42%, 39.29%, and 36.29%. The differences in soil particle sizes can lead to different simulation results[24]. In existing studies, spherical particles of equal diameter are widely used to replace irregular soil particles[25-29]. However, only a few studies have used non-equal diameter particles to replace irregular soil particles[30,31]. Using isodiametric spherical particles has the advantages of fast computation speed and relatively small simulation errors, while using non-isodiametric particles can more accurately simulate actual soil particles and improve simulation reliability, but this significantly increases computation time. In this study, non-isodiametric particles were used to simulate clay particles. Therefore, the simulation test set the soil particle sizes and percentages as follows: 5 mm particles at 24.42%, 3 mm particles at 39.29%, and 1 mm particles at 36.29%. To improve the simulation test speed, spherical particles in EDEM software (2022.3, DEM-Solutions Ltd., UK) were used to replace the irregular clay particles in HAMA.

2.1.2 Bonding V2 and JKR V2 contact models

To enhance the accuracy of simulating clay in HAMA, Bonding V2 and JKR V2 contact models (Figure 2a) were proposed, based on the complementary characteristics of the Bonding V2 and JKR V2 contact models. On one hand, HAMA are predominantly composed of wet-sticky particles and aggregated soils. During the seeding operation, the clay-furrow opening devices interaction is complex and variable. When the clay is impacted by the furrow opening devices, it fractures, and the original bonding forces between the clay particles are lost and will not be re-established. The Bonding V2 contact model can successfully simulate this destructive behavior[32]. When bonding occurs between particles, the total force and torque experienced by the clay particles are represented by Fi and Mi, respectively.

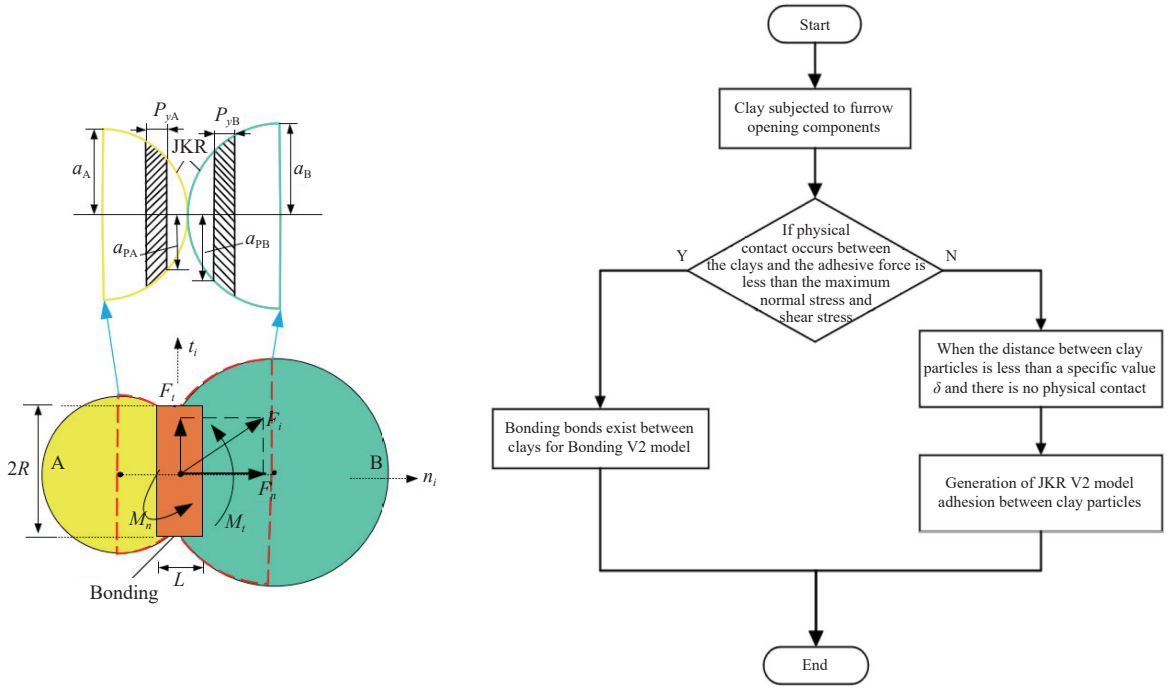

a. Bonding V2 and JKR V2 contact model principle b. Bonding V2 and JKR V2 contact model flow chart

Figure 2 Bonding V2 and JKR V2 contact models

$$\delta F_n = -v_n S_n A_b \delta t \quad (1)$$

$$\delta F_t = -v_t S_t A_b \delta_t \quad (2)$$

$$\delta M_n = -\omega_n S_t J \delta_t \quad (3)$$

$$\delta M_t = -\omega_t S_n \frac{J}{2} \delta_t \quad (4)$$

In which

$$A_b = \pi R_b^2 \quad (5)$$

$$J = \frac{1}{2}\pi R_b^4 \quad (6)$$

When the applied force on the bonding joint surpasses the threshold, the bonding can no longer maintain its connection. It will break, which means that

$$\sigma_{\max} < \frac{-F_n}{A_b} + \frac{2M_t}{J} R_b \quad (7)$$

$$\tau_{\max} < \frac{-F_n}{A_b} + \frac{M_n}{J} R_b \quad (8)$$

$$R_b = \lambda \cdot \min(R_1, R_2) \quad (9)$$

where, δF_n represents the normal force at a single time step, N; v_n is the normal velocity, m/s; S_n denotes the normal stiffness per unit area, N/m^3; A_b is the bond cross-sectional area, mm^2; δ_t is the time step, s; δF_t indicates the tangential force at a single time step, N; v_t is the tangential velocity, m/s; S_t is the tangential stiffness per unit area, N/m^3; δM_n is the normal moment at a single time step, N/m; J is the moment of inertia, m^4; δM_t is the tangential moment at a single time step, N/m; $\sigma_{\max}$ is the critical normal stress, Pa; $\tau_{\max}$ is the critical shear stress, Pa; λ is the bond radius coefficient, default value is 1.1[12,31]; ω_n is the normal angular velocity, rad/s; ω_t is the tangential angular velocity, rad/s.

On the other hand, due to the wet adhesion properties of clay in HAMA, when the distance between two contacting particles is less than a specific value, a certain adhesive force is generated and persists until the distance between them exceeds this value. In the discrete element model, the cohesive JKR V2 contact model can accurately simulate viscous soils, wet granules, and other viscous aggregates and moist particles, better demonstrating the interactions

between particles and their viscoelastic properties[8,33,34]. When two particles are in contact, the JKR V2 contact model normal elastic force is:

$$F_{JKR}=\frac{4\left(\frac{1-V_1^2}{E_1}+\frac{1-V_2^2}{E_2}\right)a^3}{3\left(\frac{1}{R_1}+\frac{1}{R_2}\right)}-4\sqrt{\pi\left(\frac{1-V_1^2}{E_1}+\frac{1-V_2^2}{E_2}\right)\gamma a^3} \quad (10)$$

$$\delta=\frac{\alpha^2}{R^*}-\sqrt{\frac{4\pi\gamma\alpha}{E^*}} \quad (11)$$

$$\gamma=\gamma_1+\gamma_2 \quad (12)$$

The cohesive force reaches its maximum value when the particles are not in contact and the gap is less than δ.

$$\alpha_c=\left[\frac{9\pi\gamma\left(\frac{1}{R_1}+\frac{1}{R_2}\right)^2}{2\left(\frac{1-V_1^2}{E_1}+\frac{1-V_2^2}{E_2}\right)}-\left(\frac{3}{4}-\frac{1}{\sqrt{2}}\right)\right]^{\frac{1}{3}} \quad (13)$$

$$F_{JKR}=-\frac{3}{2}\pi\gamma\left(\frac{1}{R_1}+\frac{1}{R_2}\right) \quad (14)$$

where, F_{JKR} represents the JKR normal elastic force, N; γ_1 and γ_2 are the surface energies of the two particles, J; V_1 and V_2 are the elastic moduli of the two particles, MPa; R_1 and R_2 are the radius of the two particles, mm; α is the radius of the contact circle, m; δ is the gap between the two particles, m; δ_c is the maximum gap, m.

When the clay is subjected to the destructive action of the furrow opening component, the bonding bond between the clays will break, and after the bonding bond breaks, the adhesive force will be formed when the distance between the clay particles is less than a specific value δ and there is no physical contact. The Bonding V2 and JKR V2 model switching logic flowchart is shown in Figure 2b.

From the above analysis, it can be seen that the traditional JKR model considers the effect of surface energy on the normal elasticity of the JKR V2 contact model, but does not take into account the effect of viscous dissipation of clay in hilly mountainous areas. In this study, the JKR V2 contact model is used to further accurately express the discrete elemental properties of clay in HAMA. The Bonding V2 and JKR V2 models were used to simulate the clay sloughing and clay adhesion properties in hilly mountainous areas, and the JKR V2 model was added between the clay-trenching components for simulating the adhesion relationship between the clay and the trenching components.

2.1.3 Intrinsic material parameters

The intrinsic parameters of clay in HAMA and 65Mn were obtained through literature review and test calibration, as listed in Table 1.

Table 1 Clay and 65Mn intrinsic parameters

Parameter	Value	Source
Clay particle density/kg·m^{-3}	1689	Test obtained
Clay Poisson's ratio	0.4	[8]
Clay elastic modulus/Pa	1×10^9	
65Mn density/kg·m^{-3}	7850	[16]
65Mn Poisson's ratio	0.3	
65Mn elastic modulus/Pa	7.9×10^{10}	

2.2 Calibration of contact parameters for the JKR V2 contact model

2.2.1 Calibration of clay-clay contact parameters

(1) Physical test of clay AOR

The clay AOR test was conducted using the cylindrical lifting method [35] (Wu et al., 2002). Figure 3a shows the AOR devices, comprising a universal testing machine (Model MTS Exceed E43.104, manufactured by MTS Systems (China) Co., Ltd.), a Q235 material cylinder (210 mm in height × 70 mm inner diameter) and a 300 mm square baseplate. Ten clay samples were tested in total. For the test, the cylinder is first secured to the lifting mechanism of the universal testing machine using a custom-made clamping device, ensuring that the cylinder vertically contacts the receiving tray. Clay, previously sieved, is filled into the cylinder until level with the top of the cylinder, and the bottom of the cylinder touches a square steel plate (250 mm in length × 250 mm in width). During the test, the cylinder was lifted vertically upward at a speed of 8.33 mm/s, allowing the clay to naturally fall and accumulate under gravity before data collection. Each soil sample is repeated three times.

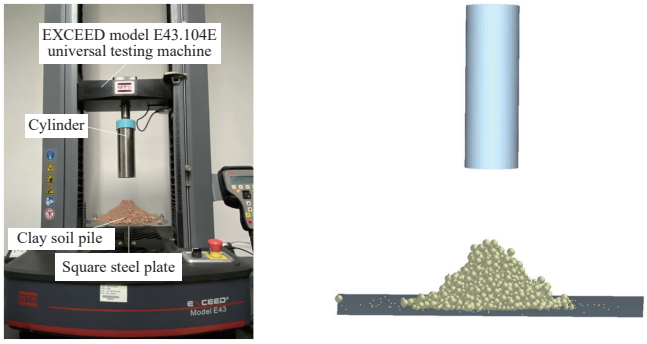

a. Physical test b. Simulation test

Figure 3 Clay AOR test

(2) Simulation test of clay AOR

Figure 3b shows the simulation test for clay AOR. The clay AOR is used as the response value, and a CCD with four factors and three levels is employed[8,11,36]. According to the recommended parameter ranges of the GEMM (Generic EDEM Material Model) and with reference to relevant studies[8,15], the simulation test design for the clay AOR is listed in Table 2.

Table 2 Clay AOR simulation test

Test No.	JKR surface energy X_1/J·m^{-2}	Clay-clay static friction coefficient X_2	Clay-clay rolling friction coefficient X_3	Clay-clay restitution coefficient X_4
–1	6	0.2	0.05	0.15
0	8	0.56	0.125	0.45
1	10	0.92	0.2	0.75

2.2.2 Calibration of clay-65Mn contact parameters

To determine the clay on 65Mn material static friction coefficient for the seeder's furrow opening devices[37], a static friction test was conducted using clay from HAMA. Additionally, a rolling friction simulation test was employed to calibrate the contact parameters and JKR surface energy of clay on 65Mn.

(1) Clay static friction test

A static friction test bench was set up to test the clay against 65Mn static friction coefficient, which is shown in Figure 4. Before the test, clay was shaped into 10 mm cubic blocks. An inclinometer was used to measure the angle at which the clay block started to slide. This test was repeated 20 times. The corresponding static

friction coefficients were calculated using Equations (15) and (16). The measured clay and 65Mn static friction coefficient range was found to be 0.2-0.7.

$$\begin{cases} F_x = G_1 \sin\theta_1 \\ F_y = G_1 \cos\theta_1 \\ F_x - f_1 = 0 \\ F_y - N_1 = 0 \\ f_1 = \mu_1 F_y \end{cases} \quad (15)$$

$$\mu_1 = \frac{f_1}{F_y} = \frac{F_x}{F_y} = \frac{G\sin\theta_1}{G\cos\theta_1} = \tan\theta_1 \quad (16)$$

where, F_x is the tensile force, N; F_y is the compressive force, N; G_1 is the gravitational force, N; f_1 is the frictional force, N; N_1 is the normal force, N; μ_1 is the static friction coefficient; and θ_1 is the slope angle, (°).

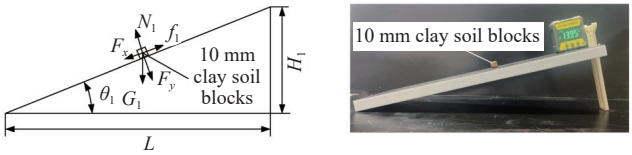

a. Principle of static friction measurement

b. Static friction test rig

Figure 4 Static friction test rig and its measurement principle

(2) Clay-65Mn rolling friction physical test

As shown in Figure 5, the clay-65Mn rolling friction physical test was conducted using a rolling friction test bench constructed with a 65Mn plate. The test bench consists of a 65Mn inclined plane (200 mm long × 100 mm wide) and a 65Mn flat plane (400 mm long × 10 mm wide), with the height H_2 at the end of the 65Mn inclined plane being 29 mm. The basic steps of the test are as follows: Place a clay ball (R=5 mm) at the initial position of the inclined plane (H_2 = 29 mm), allowing the clay ball to roll freely along the slope until it stops. Use a ruler to measure the clay ball horizontal rolling distance S_2. The test value of the clay ball rolling in a straight line is taken as the final test value, and this is repeated 10 times. According to Equation (17), the clay-65Mn rolling friction coefficient is determined to be between 0.04 and 0.08.

$$G_2 H_2 = \mu_2 G_2 (S_1 \cos\theta_2 + S_2) \quad (17)$$

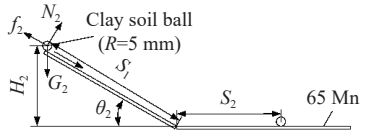

a. Principle of clay-65Mn rolling friction test

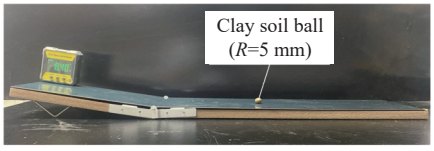

b. Clay-65Mn rolling friction test rig

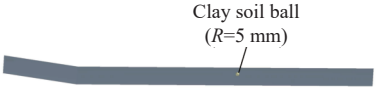

c. Clay-65Mn rolling friction EDEM simulation test

Figure 5 Clay-65Mn rolling friction test rig and measurement principle

where, G_2 is the gravity of the clay ball, N; f_2 is the friction of the clay ball, N; N_2 is the supporting force of the clay ball, N; H_2 is the initial height of the clay ball, mm; S_1 is the linear distance the clay ball rolls freely on the 65Mn inclined plane, mm; S_2 is the linear distance the clay ball rolls on the 65Mn flat plane, mm; θ_2 is the angle of the 65Mn inclined plane, (°); μ_2 is the clay-65Mn rolling friction coefficient.

(3) Clay-65Mn rolling friction simulation test

Figure 5c shows the clay-65Mn rolling friction EDEM simulation test. The simulation test parameters were set according to the physical test settings. Based on the recommended parameters for 65Mn in GEMM, as well as the results from the preliminary simulation tests and physical tests, a four-factor, three-level simulation test plan was formulated for the clay-65Mn rolling friction simulation test (Table 3).

Table 3 Clay-65Mn rolling friction simulation test

Test No.	JKR surface energy X_5/J·m^{-2}	Clay-65Mn static friction coefficient X_6	Clay-65Mn rolling friction coefficient X_7	Clay-65Mn restitution coefficient X_8
–1	2	0.2	0.04	0.2
0	7	0.45	0.06	0.4
1	12	0.7	0.08	0.6

2.3 Calibration of bonding parameters for the Bonding V2 contact model

2.3.1 Clay compaction physical calibration test

The clay compaction physical test was conducted at the same location where the clay samples were collected. A clay compaction meter (FieldScout SC900, USA) was used to randomly designate the test area (Figure 6c) for detection (Figure 6a). During testing, the clay surface was leveled, and a cover plate was placed on top. The clay compaction meter was then moved vertically downward at a uniform speed, and the clay compaction values at various clay depths were recorded (Figure 6b). Tested 25 times in total, the average clay compaction value at a depth of 5 cm below the surface was calculated to be 310.7 kPa.

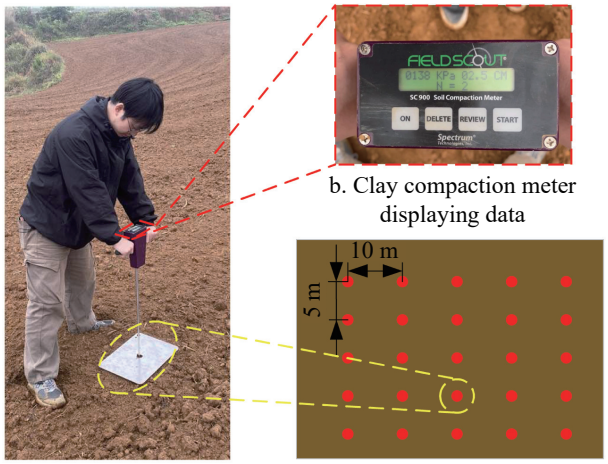

a. Clay compaction measurement site

b. Clay compaction meter displaying data

c. Distribution of clay compaction sampling points

Figure 6 Clay compaction measurement

2.3.2 Plackett-Burman test

The PB test takes the clay compaction as the response value. The four parameters in the PB test are represented by the letters X_9 to X_{12}, with each parameter set at high, low, and medium levels, denoted by the codes 1, –1, and 0, respectively. The calculated Bond disk scale is 1.1[12]. The overall tests of 12 groups were conducted, each duplicated three times. The PB test parameters are listed in Table 4.

Table 4 PB test parameters

Parameters	Low level (–1)	High level (+1)
Normal stiffness per unit area X_9/N·m^{-3}	1×10^7	7×10^7
Tangential stiffness per unit area X_{10}/N·m^{-3}	5×10^5	5×10^6
Critical normal stress X_{11}/Pa	5×10^5	5×10^6
Critical shear stress X_{12}/Pa	5×10^3	5×10^4

In accordance with the calibrated contact parameters and HAMA clay JKR surface energy and the 65Mn material of the furrow opening devices, a 3D model of the cone (125 mm high × 10 mm diameter, made of steel) was drawn according to the actual size of the clay compaction meter. Using the Volume Pack function in EDEM, a clay tank (400 mm long × 400 mm wide × 300 mm high) was quickly generated. After importing the 3D model of the cone into EDEM, a clay compaction measurement simulation test was conducted. The cone moves vertically downward at a constant speed of 0.06 m/s until the tip of the cone completely enters the clay, ending the motion. The simulation test is consistent with the physical test, as shown in Figure 7. The calculation formula for clay compaction P is:

$$P = \frac{F}{A} \tag{18}$$

where, F represents the maximum force exerted on the cone when it stops moving, N; A represents the cross-sectional area that is level with the clay surface when the cone stops moving, m^2.

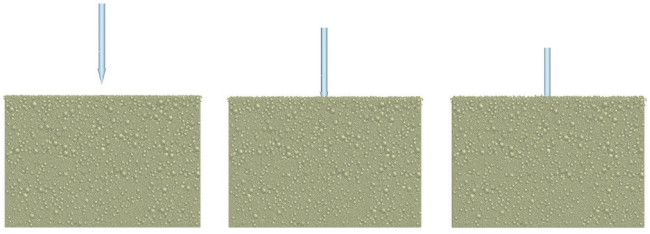

a. Cone before penetrating the clay b. Cone penetrating the clay c. Cone completely enters the clay

Figure 7 Clay compaction simulation test

2.3.3 Steepest climbing test

Table 7 shows the steepest climbing test scheme and results. The test factors include significant variables such as normal stiffness per unit area X_9, critical shear stress X_{12}, and shear stiffness per unit area X_{10}. The sign of the steepest climbing test is the relative error δ of both the actual clay compaction values and the simulated ones. The test is divided into seven groups, with each group repeated three times. The equation for the relative error δ is as follows:

$$\delta = \frac{|P_s - P_x|}{P_s} \times 100\% \tag{19}$$

where, δ is the simulated clay compaction value and the actual value relative error; P_s is the actual clay compaction value, kPa; P_x is the simulated clay compaction value, kPa;

2.3.4 Box-Behnken Design test

To further optimize the bonding parameters, a BBD test plan was designed, as shown in Table 8. The non-significant parameter, critical normal stress X_{11}, is set to 2.75×10^6 Pa. The significant factors are set as follows: normal stiffness per unit area X_9 ranges from 3×10^7 to 5×10^7 N/m^3, critical shear stress X_{12} ranges from 2×10^4 to 3.5×10^4 Pa, and shear stiffness per unit area X_{10} ranges from 2×10^6 to 3.5×10^6 N/m^3. The test includes five center points to estimate error, and each test group is repeated three times.

2.4 Direct shear validation test

Figure 8a shows the HAMA clay direct shear physical test. During the test, the collected clay is located in a shear box. The clay parameters and test parameters are set in the Geotechnical Software (DS7, ELE International, United Kingdom). After calibrating the sensors, a vertical pressure of 200 kPa is applied to compact the clay. The shear box then shears at a 0.2 mm/min constant speed. During this process, the horizontal force on the shear box is observed. The test is repeated three times. After the test, the test data is saved.

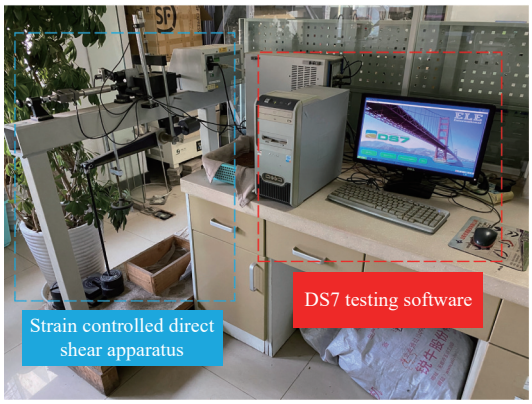

a. Claydirect shear physical test

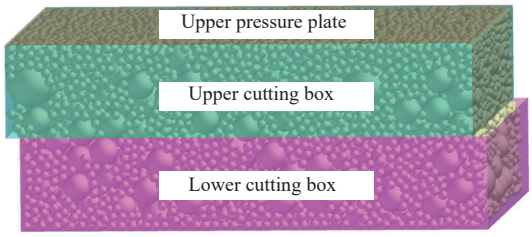

b. Claydirect shear simulation verification test

Figure 8 Clay direct shear physical and simulation verification test

As shown in Figure 8b, the direct shear simulation test was conducted using the Bonding V2 and JKR V2 contact models, with the Bond V2 contact model and JKR V2 model used as control groups for comparison to validate the advantages of the Bonding V2 and JKR V2 contact models. The test was repeated three times.

2.5 Furrowing operation validation test

In order to further verify the accuracy and reliability of the contact model parameters of Bonding V2 and JKR V2, MBD-DEM coupled simulation and field validation tests were conducted. The field test was conducted in May 2024 in Jinbi Town, Qianxi City, Guizhou Province. For the field validation test of furrowing operation (Figure 9), the rotary plowed post-tillage plowing land with a surface slope of 15°±1° was selected, with the physical properties of the surface soil remaining the same, and with an average value of clay compaction of 310.7 kPa. The test was conducted using a Dongfanghong MF904 tractor as the traction power, and the furrowing component carrier was selected to be a 2BMXE-2C planter, with an operating speed of 5 km/h and spring initial increment of 30 mm as the field test parameters for furrowing operation. Uphill and downhill furrowing operations were carried out respectively, and the test was repeated three times each. The simulation test was consistent with the field test parameters. In the MBD-DEM coupled simulation test, the EDEM and RecurDyn simulation time step was set to 0.0001 s, and the save time interval was 0.2 s. The statistical formulas for the trenching depth operation performance of the MBD-DEM coupled simulation and the field test are as follows:

a. Uphill 15° b. Downhill 15°

Figure 9 Simulation and field validation tests of furrow opening operation

$$\bar{d} = \frac{\sum d_i}{h_0} \tag{20}$$

$$H = \frac{h_1}{h_0} \times 100\% \tag{21}$$

$$V = \frac{\sqrt{\frac{\sum (d_i - \bar{d})^2}{h_0}}}{\bar{d}} \times 100\% \tag{22}$$

where, $\bar{d}$ represents the mean of the furrow opening depth; H is the qualified rate of furrow opening depth, which refers to the percentage of qualified furrow opening depth within ±5 mm error range relative to the target furrow opening depth of 50 mm; V is the coefficient of variation of furrow opening depth, and h_0 is the total number of furrow opening depths; d_i is the i-th value of the furrow opening depth; h_1 is the qualified furrow opening depth.

In the simulation test, the EDEM and RecurDyn simulation time steps were set to 0.0001 s, with a save interval of 0.2 s. Data on the furrow opening depth were collected within a stable range during the MBD-DEM coupling simulation process, and the furrow opening depth was measured during the coupling simulation test.

3 Results and discussion

3.1 Results of the calibration test for the contact parameters of the JKR V2 contact models

3.1.1 Clay-clay contact parameter calibration test

MATLAB (R2023b, MathWorks, Natick, MA, USA) was used to sequentially process the physical and simulation test results (Figure 10a). The processing steps included binarization, color inversion, closing operations for hole filling, boundary curve extraction, and data segmentation and export. Figure 10b and Figure 10c show the boundary was then linearly fitted using Origin (2024, OriginLab Corporation, Northampton, MA, USA) to obtain the fitted linear equations. ρ_L and ρ_R represent the AOR on the left and right sides, and these fitted equations were used for the left and right profiles of the AOR and for linear fitting. After averaging ρ_L and ρ_R, the clay AOR from the physical test is found to be 34.85°. Table 5 lists the clay AOR simulation test results.

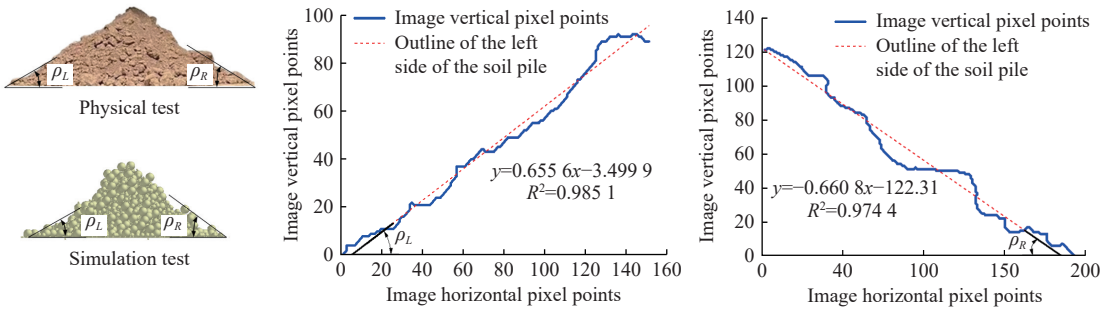

a. Physical andsimulation test b. The left AOR fitting curve c. The right AOR fitting curve

Figure 10 Clay AOR test

Quadratic regression equation of clay AOR:

$$\begin{aligned} Y_1 =& 41.75 + 5.29X_1 + 12.69X_2 + 12.16X_3 - 2.66X_4 - \\ & 0.78X_1X_2 - 0.99X_1X_3 + 1.13X_1X_4 + 5.80X_2X_3 + 0.84X_2X_4 + \\ & 1.22X_3X_4 - 0.67X_1^2 - 17.16X_2^2 - 4.94X_3^2 - 0.63X_4^2 \end{aligned} \tag{23}$$

The analysis of variance (ANOVA) table is shown in Table 6. The p-value of the model is less than 0.0001, indicating that the model is significant. The coefficient of determination R^2 is 0.8788, indicating high accuracy of the regression model. Meanwhile, the p-value of the misfit term was greater than 0.05 and the difference was not significant, indicating that the model had a good fit. Among all the test factors, except for the coefficient of recovery between clays, all the other factors had a significant effect on the stacking angle (p<0.05), and the degree of importance of each factor was: X_2>X_3>X_1>X_4.

Using the measured AOR of 34.85° from physical tests as the target for optimization, the optimization results are listed in Table 7.

3.1.2 Clay-65Mn contact parameter calibration test

The clay and 65Mn rolling friction simulation results are shown in Table 8.

The quadratic regression equation of clay-65Mn is as follows:

$$\begin{aligned} Y_2 =& 246.99 - 8.26X_5 - 3.04X_6 - 143.27X_7 - 1.93X_8 + \\ & 0.28X_5X_6 + 0.18X_5X_7 - 0.85X_5X_8 - 1.11X_6X_7 - 4.62X_6X_8 + \\ & 0.49X_7X_8 + 2.05X_5^2 + 6.48X_6^2 + 37.89X_7^2 - 0.7289X_8^2 \end{aligned} \tag{24}$$

The ANOVA for the soil-65Mn test is listed in Table 9. The

Table 5 Clay AOR simulation test results

Test No.	JKR surface energy X_1/J·m^{-2}	Clay-clay static friction coefficient X_2	Clay-clay rolling friction coefficient X_3	Clay-clay restitution coefficient X_4	Clay AOR/(°)
1	8	0.92	0.2	0.35	40.55
2	8	0.92	0.05	0.35	18.39
3	8	0.56	0.2	0.15	51.90
4	6	0.56	0.2	0.35	47.57
5	10	0.56	0.2	0.35	58.18
6	6	0.56	0.125	0.15	36.53
7	8	0.92	0.125	0.55	36.25
8	6	0.56	0.125	0.55	27.85
9	10	0.56	0.05	0.35	28.25
10	10	0.56	0.125	0.15	50.84
11	10	0.92	0.125	0.35	37.30
12	8	0.56	0.125	0.35	39.19
13	10	0.56	0.125	0.55	46.67
14	8	0.56	0.2	0.55	49.34
15	8	0.56	0.05	0.15	23.86
16	8	0.56	0.125	0.35	41.80
17	8	0.92	0.125	0.15	42.47
18	6	0.56	0.05	0.35	13.68
19	8	0.2	0.05	0.35	10.39
20	8	0.56	0.125	0.35	42.74
21	8	0.2	0.2	0.35	9.36
22	8	0.56	0.05	0.55	16.41
23	8	0.56	0.125	0.35	35.66
24	6	0.92	0.125	0.35	36.29
25	10	0.2	0.125	0.35	11.53
26	8	0.2	0.125	0.15	11.56
27	8	0.56	0.125	0.35	49.38
28	6	0.2	0.125	0.35	7.40
29	8	0.2	0.125	0.55	8.69

Table 6 ANOVA for the regression model of clay AOR

Source	Sum of squares	Degree of freedom	Mean square	F	p
Model	6311.51	14	450.82	11.36	< 0.0001
X_1	335.49	1	335.49	8.45	0.0115
X_2	1933.45	1	1933.45	48.71	< 0.0001
X_3	1774.39	1	1774.39	44.70	< 0.0001
X_4	85.07	1	85.07	2.14	0.1653
X_1X_2	2.43	1	2.43	0.0613	0.8080
X_1X_3	3.92	1	3.92	0.0988	0.7579
X_1X_4	5.09	1	5.09	0.1281	0.7257
X_2X_3	134.44	1	134.44	3.39	0.0870
X_2X_4	2.81	1	2.81	0.0707	0.7942
X_3X_4	5.98	1	5.98	0.1506	0.7038
X_1^2	2.90	1	2.90	0.0730	0.7910
X_2^2	1909.38	1	1909.38	48.11	< 0.0001
X_3^2	158.58	1	158.58	4.00	0.0654
X_4^2	2.60	1	2.60	0.0655	0.8017
Residual	555.69	14	39.69		
Lack of fit	452.84	10	45.28	1.76	0.3080
Pure error	102.84	4	25.71		
Cor total	6867.20	28			

Note: $p\geq0.05$ (not significant); $0.01\leq p<0.05$ (significant); $p<0.01$ (highly significant).

model p-value is less than 0.0001, indicating that the model is highly significant. The coefficient of determination R^2 is 0.9947, indicating high accuracy of the regression model. Meanwhile, the p-value of the misfit term is greater than 0.05, and the difference is not significant, indicating that the model has a good fit. Except for the soil-65Mn static friction coefficient and the coefficient of recovery, which are not significant ($p>0.05$), the rest of the factors have a significant effect on the rolling distance, and the clay-65Mn rolling friction coefficient X_7 has a highly significant effect ($p<0.0001$). From the F-value, it can be seen that the influence of each factor on rolling distance is $X_7>X_5>X_6>X_8$ in descending order.

The optimization was carried out with the goal of achieving the rolling distance of 197.97±9.23 mm, as determined in the rolling friction physical test results of Section 3.1.1. The optimization results are shown in Table 10.

Table 7 Parameters of clay-clay contact model

Parameters	Value
JKR surface energy X_1/J·m^{-2}	6.520
Clay-clay static friction coefficient X_2	0.742
Clay-clay rolling friction coefficient X_3	0.104
Clay-clay restitution coefficient X_4	0.355

Table 8 Clay-65Mn rolling friction simulation test results

Test No.	JKR surface energy X_5/(J·m^{-2})	Clay-65Mn Static friction coefficient X_6	Clay-65Mn Rolling friction coefficient X_7	Clay-65Mn restitution coefficient X_8	Clay rolling distance/mm
1	12	0.2	0.06	0.4	253.31
2	2	0.45	0.04	0.4	444.48
3	7	0.7	0.04	0.4	432.4
4	2	0.45	0.08	0.4	148.16
5	12	0.45	0.08	0.4	130.53
6	7	0.45	0.06	0.4	242.77
7	7	0.45	0.04	0.6	417.72
8	7	0.7	0.06	0.2	268.51
9	7	0.45	0.08	0.6	147.51
10	2	0.45	0.06	0.2	264.53
11	7	0.45	0.06	0.4	246.62
12	7	0.45	0.06	0.4	252.82
13	2	0.45	0.06	0.6	262.74
14	12	0.7	0.06	0.4	244.28
15	7	0.2	0.06	0.6	246.99
16	7	0.2	0.06	0.2	249.43
17	2	0.2	0.06	0.4	260.66
18	7	0.45	0.08	0.2	142.96
19	7	0.45	0.06	0.4	239.49
20	12	0.45	0.06	0.6	236.28
21	12	0.45	0.06	0.2	241.47
22	7	0.2	0.04	0.4	448.68
23	2	0.7	0.06	0.4	250.52
24	7	0.45	0.04	0.2	415.12
25	12	0.45	0.04	0.4	426.13
26	7	0.45	0.06	0.4	253.26
27	7	0.7	0.06	0.6	247.59
28	7	0.7	0.08	0.4	137.71
29	7	0.2	0.08	0.4	158.43

3.2 Results of the calibration test for the bonding parameters of the Bonding V2 contact model

3.2.1 PB test

The PB test plan and results are listed in Table 11. As seen from Table 11, the clay compaction varies significantly within a certain range with changes in the levels of each factor. The ANOVA results are shown in Table 12. Simulation parameters X_9 and X_{12} have a significant impact on clay compaction ($p<0.05$). Considering the magnitude of their influence, calibration tests for

bonding parameters X_9, X_{12}, and X_{10} will be conducted in the subsequent test design. The remaining parameter will be set to its median value, $X_{11} = 2.75\times10^6$ Pa.

Table 9 ANOVA for the regression model of rolling distance on 65Mn plate

Source	Sum of squares	Degree of freedom	Mean square	F	p
Model	2.572E+05	14	18 373.31	188.11	< 0.0001
X_5	818.24	1	818.24	8.38	0.0118
X_6	110.96	1	110.96	1.14	0.3045
X_7	2.463E+05	1	2.463E+05	2521.80	< 0.0001
X_8	44.81	1	44.81	0.4588	0.5092
X_5X_6	0.3080	1	0.3080	0.0032	0.9560
X_5X_7	0.1296	1	0.1296	0.0013	0.9715
X_5X_8	2.89	1	2.89	0.0296	0.8659
X_6X_7	4.93	1	4.93	0.0505	0.8255
X_6X_8	85.38	1	85.38	0.8741	0.3657
X_7X_8	0.9506	1	0.9506	0.0097	0.9228
X_5^2	27.29	1	27.29	0.2794	0.6054
X_6^2	272.25	1	272.25	2.79	0.1172
X_7^2	9314.10	1	9314.10	95.36	< 0.0001
X_8^2	3.45	1	3.45	0.0353	0.8537
Residual	1367.43	14	97.67		
Lack of fit	1219.93	10	121.99	3.31	0.1301
Pure error	147.50	4	36.87		
Cor total	2.586E+05	28			

Note: $p\geq0.05$ (insignificant); $0.01\leq p<0.05$ (significant); $p<0.01$ (highly significant).

Table 10 Parameters of clay-65Mn contact model

Parameters	Value
JKR surface energy X_5/J·m^{-2}	2.798
Clay-65Mn static friction coefficient X_6	0.438
Clay-65Mn rolling friction coefficient X_7	0.069
Clay-65Mn restitution coefficient X_8	0.238

Table 11 Results of the PB test

Test No.	X_9	X_{10}	X_{11}	X_{12}	Clay compaction/kPa
1	–1	–1	–1	1	105.95
2	–1	1	1	–1	129.80
3	–1	1	1	1	182.43
4	1	1	–1	–1	203.46
5	1	–1	–1	–1	297.81
6	–1	–1	1	–1	105.95
7	1	–1	1	1	287.29
8	1	1	1	–1	202.51
9	1	–1	1	1	279.11
10	–1	–1	–1	–1	95.62
11	1	1	–1	1	452.99
12	–1	1	–1	1	253.10

Table 12 ANOVA of PB test

Parameter	Effect	Sum of squares	p
X_5	141.72	60 253.78	0.0062
X_6	42.09	5315.94	0.2884
X_7	–36.97	4101.00	0.3466
X_8	87.62	23 032.20	0.0481

3.2.2 Steepest climbing test

The results of the steepest climbing test are shown in Table 13. The normal stiffness per unit area X_9, critical shear stress X_{12}, and the tangential stiffness per unit area X_{10} are positively correlated with clay compaction. Among the groups, Group 4 has the smallest relative error to the target clay compaction value of 316 kPa, with a deviation of –2.90%. The level intervals of 4 and 6 are selected as the factor ranges for the BBD test.

Table 13 Scheme and results of the steepest climbing test

Test No.	X_9/N·m^{-3}	X_{12}/Pa	X_{10}/N·m^{-3}	Soil compaction/kPa	Relative error δ/%
1	1×10^7	5×10^3	5×10^5	105.95	–65.90%
2	2×10^7	1.25×10^4	1.25×10^6	191.67	–38.31%
3	3×10^7	2×10^4	2×10^6	264.02	–15.02%
4	4×10^7	2.75×10^4	2.75×10^6	301.69	–2.90%
5	5×10^7	3.5×10^4	3.5×10^6	349.85	12.60%
6	6×10^7	4.25×10^4	4.25×10^6	407.04	31.01%
7	7×10^7	5×10^4	5×10^6	452.99	45.80%

3.2.3 BBD test

The BBD test results are listed in Table 14.

Table 14 BBD test results

Test No.	X_9/N·m^{-3}	X_{12}/Pa	X_{10}/N·m^{-3}	Soil compaction/kPa
1	0 (4×10^7)	–1 (2×10^4)	–1 (2×10^6)	269.43
2	1 (5×10^7)	0 (2.75×10^4)	1 (3.5×10^6)	339.62
3	0	0	0 (2.75×10^6)	322.23
4	0	0	0	331.69
5	1	–1	0	351.56
6	–1 (3×10^7)	–1	0	284.22
7	0	0	0	304.54
8	0	–1	1	356.21
9	0	1 (3.5×10^4)	1	357.26
10	–1	0	1	327.00
11	–1	0	–1	264.02
12	0	0	0	310.54
13	1	0	–1	286.72
14	0	1	–1	262.97
15	1	1	0	328.24
16	0	0	0	323.61
17	–1	1	0	284.22

The quadratic regression equation of soil compaction is as follows:

$$Y_3 = 318.52 + 18.33X_9 - 3.59X_{12} + 37.12X_{10} - 5.83X_9X_{12} - 2.52X_9X_{10} + 1.88X_{12}X_{10} - 6.80X_9^2 + 0.3340X_{12}^2 - 7.39X_{10}^2 \quad (25)$$

The results of the analysis of variance (ANOVA) are shown in Table 15. The model's p-value is 0.0117, which is less than 0.05, indicating that the model is significant. The coefficient of determination, R^2, is 0.8910, suggesting that the regression model has high accuracy. Additionally, the LOF p-value is 0.121, greater than 0.05, indicating that the lack-of-fit is not significant and that the model has good fitting performance within the regression range. Except for critical tangential stress (X_{12}), which has an insignificant effect on clay compaction ($p>0.05$), all other factors significantly affect clay compaction ($p<0.05$). Among these, unit area tangential stiffness (X_{10}) brings about a major impact on clay compaction ($p<0.01$), and unit area normal stiffness (X_9) has a significant effect on clay compaction ($0.01\leq p<0.05$). According to the F-value, the factors affecting clay compaction in descending order are $X_{10} > X_9 > X_{12}$.

Table 15 BBD test ANOVA

Source	Sum of squares	Degree of freedom	Mean square	F	p
Model	14 438.19	9	1604.24	6.36	0.0117
X_9	2688.5	1	2688.5	10.65	0.0138
X_{12}	103.24	1	103.24	0.4092	0.5428
X_{10}	11 022.41	1	11 022.41	43.68	0.0003
X_9X_{12}	135.95	1	135.95	0.5388	0.4868
X_9X_{10}	25.42	1	25.42	0.1007	0.7602
$X_{12}X_{10}$	14.12	1	14.12	0.0559	0.8198
X_9^2	194.42	1	194.42	0.7705	0.4092
X_{12}^2	0.4697	1	0.4697	0.0019	0.9668
X_{10}^2	229.76	1	229.76	0.9106	0.3717
Residual	1766.29	7	252.33		
Lack of fit	1294.05	3	431.35		0.1214
Pure error	472.24	4	118.06		
Cor total	16 204.48	16			

Note: $p\geq0.05$ (not significant); $0.01\leq p<0.05$ (significant); $p<0.01$ (highly significant).

3.2.4 Interaction response analysis of regression model

Figure 11 shows the response surface and contour plots of the interaction factors X_{10} (tangential stiffness per unit area) and X_9 (normal stiffness per unit area) on soil compaction, with X_{12} (critical shear stress) fixed at 2.75×10^4 Pa. Clay compaction is positively correlated with tangential stiffness per unit area and critical shear stress. As X_{10} and X_9 increase, clay compaction tends to increase and gradually stabilizes.

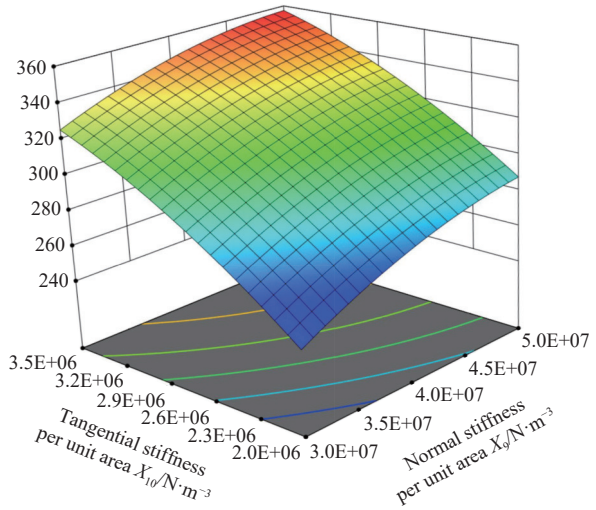

Figure 11 Response surface plot of interaction factors on clay compaction (X_{12}=2.75×10^4 Pa)

3.2.5 Determination of the optimal combination of bonding parameters

Based on the regression model's optimization for the target clay compaction of 310.7 kPa, the optimal calibration parameter combination for clay compaction is listed in Table 16.

Table 16 Parameters of clay bonding

Parameters	Value
Normal stiffness per unit area X_9/N·m^{-3}	4.71×10^7
Tangential stiffness per unit area X_{10}/N·m^{-3}	2.32×10^6
Critical normal stress X_{11}/Pa	2.75×10^6
Critical shear stress X_{12}/Pa	23 080

Simulations were conducted using the optimal bonding parameters combination, and the variation of clay compaction over time during the simulation is shown in Figure 12. The clay compaction value starts at 0 and significantly increases with the depth of the cone penetration into the clay, reaching maximum clay compaction when the cone is fully embedded. The relative error of the HAMA clay compaction values, both simulated and measured, is 1.79%. It is proven that the calibrated Bond V2 contact model can accurately simulate the bonding parameters of clay in HAMA.

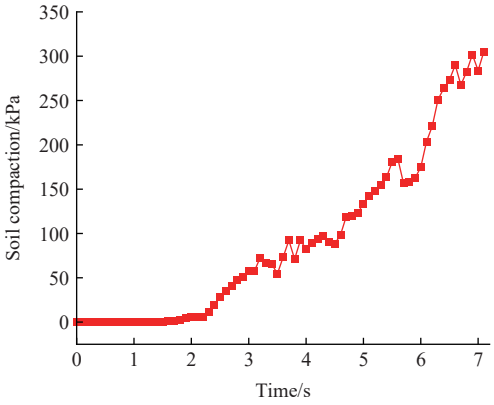

Figure 12 Process of soil compaction change

3.3 Results of the direct shear validation test for the Bonding V2 and JKR V2 contact models

As shown in Figure 13, the shear stress-displacement curves for the Bonding V2 and JKR V2 contact models simulation and the physical direct shear test are presented. The figure also includes the shear stress-displacement curves for the Bonding V2 model and the JKR V2 model alone. From the figure, it can be observed that the Bonding V2 and JKR V2 contact models closely follow the trend of the actual shear stress-displacement curve, with a maximum shear stress of 109.37 kPa, and a relative error of 4.90%, compared to the actual maximum shear stress of 104.26 kPa. In contrast, while the Bonding V2 model alone shows a generally similar trend, the error in shear stress compared to the actual data is too large. The JKR V2 model alone shows an overall trend that does not align with the actual data. Overall, the Bonding V2 and JKR V2 contact models can more accurately simulate the clay in HAMA, demonstrating the reliability of the Bonding V2 and JKR V2 contact models' simulation.

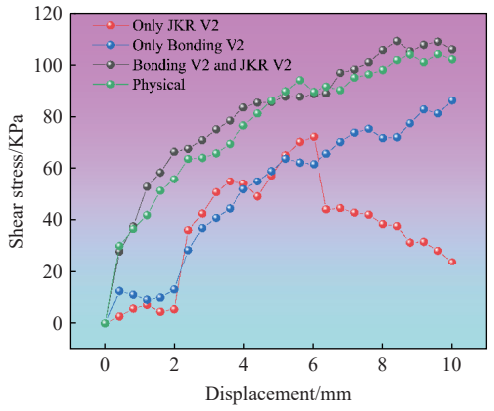

Figure 13 Physical and simulated shear stress-displacement curve for direct shear test

3.4 Optimization and validation results of furrowing operation parameters

3.4.1 Furrow operation simulation and field validation test

Figure 14 shows the data collection process during the field tests for furrowing operations. Divide one uphill and one downhill into a group, mark them continuously with yellow labels, measure them, and then proceed to the next group of measurements. In the field tests, four sampling areas were randomly selected on uphill and downhill slopes. Seven sampling points were continuously selected in each sampling area to measure the furrow opening depth, and the data were recorded. According to Equations (20)-(22), the average value, qualification rate, and coefficient of variation of the furrow opening depth could be calculated.

Figure 14 Field data collection during furrow opening operation tests

Table 18 presents the results of the field and simulation tests for furrowing operations, conducted on two typical HAMA terrains, uphill and downhill, to test the simulation accuracy of the Bonding V2 and JKR V2 contact models. As shown in Table 18, the relative errors between the average furrow opening depth from the uphill and downhill coupling simulations and the actual operations were 3.02% and 6.89%, respectively. The relative errors for the furrow opening depth qualification rate were 9.64% and 8.54%, respectively, both within 10%. The relative errors for the coefficient of variation of furrow opening depth were 13.32% and 11.62%, respectively, both within 15%. These errors are within acceptable ranges, indicating that the contact and bonding parameters of the Bonding V2 and JKR V2 contact models are consistent with the actual clay in HAMA, further validating the simulation accuracy of the Bonding V2 and JKR V2 contact models.

Table 17 Comparison of results from field and simulation tests for furrowing operations

Test indicators		Uphill (15°)	Downhill (–15°)
The average of furrow opening depth/mm	Simulation	50.02	50.27
	Field	51.58	53.99
	Relative error/%	3.02	6.89
The qualification rate of furrow opening depth/%	Simulation	97.78	98.39
	Field	89.18	90.65
	Relative error/%	9.64	8.54
The CV of furrow opening depth/%	Simulation	4.75	6.31
	Field	5.48	7.14
	Relative error/%	13.32	11.62

3.4.2 Simulation and field test analysis of furrow opening profile

To further validate the accuracy of the Bonding JKR combination model, a comparative analysis was conducted using the furrow opening profile formed after the furrow opening operation[4,7,9,38]. As shown in Figures 15a and 15b, simulation test data were collected in EDEM, and a box with dimensions of 2000 mm in length, 450 mm in width, and 200 mm in depth was created within the data collection area. Then the box was divided into multiple square grid cells of the same width and height as the data collection area (450 mm). The entire length of the data collection area is used as the grid cell length to consider variations along the plow direction. The number of particles with centroids located within a specific grid cell was calculated for that grid cell. Loose particle boundaries (furrow opening profile) were defined by counting different numbers of particles using grid cells. The field test uses a shape-taking device to take shape (Figures 15c and 15d), records the coordinate position, and draws the profile of the furrow opening.

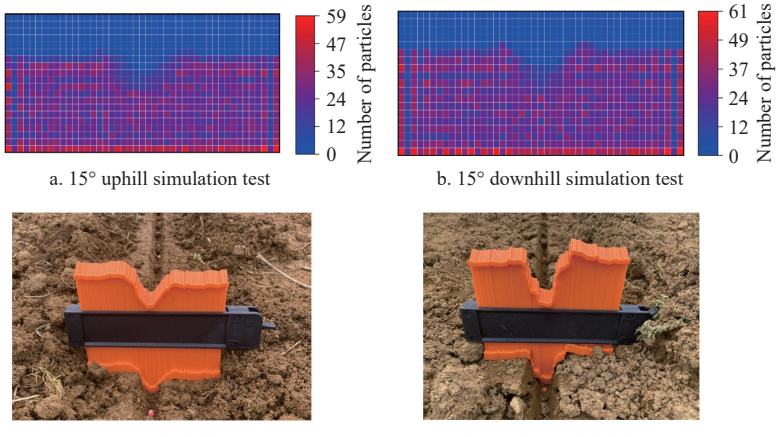

a. 15° uphill simulation test b. 15° downhill simulation test

c. 15° uphill field test d. 15° downhill field test

Figure 15 Data collection of furrow opening profile

The furrow opening depth profile obtained from simulation and field tests are shown in Figure 16. By statistically analyzing the number of particles in the simulation and field test results, the furrow opening depth profiles for uphill 15° and downhill 15° were obtained. From the boundary curves, it can be seen that the furrow depth profile obtained from simulation and field tests is basically consistent. When going uphill, the furrow opening is shallower and smaller, and the protrusions on both sides of the furrow opening are smaller. When going downhill, the furrow opening is deeper and larger, and the protrusions on both sides of the furrow opening are larger. This is because the soil is subjected to greater compression when going downhill. During on-site operations, due to the influence of actual furrow opening conditions, the furrow opening depth may be slightly deeper, and the ground on both sides of the furrow opening will first sink significantly. However, in the simulated test environment, the working conditions are relatively stable, and the clay state on both sides of the furrow opening is relatively stable.

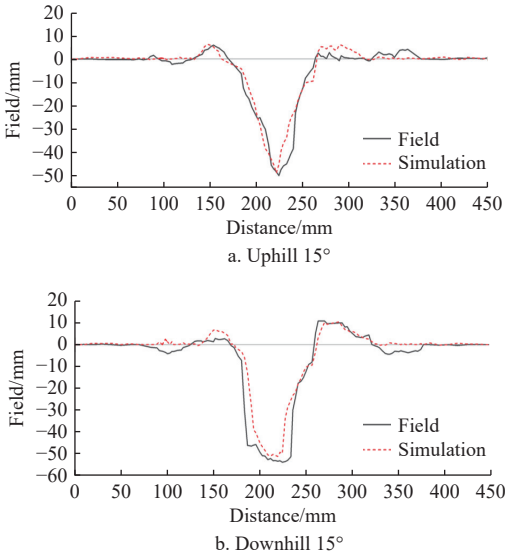

Figure 16 Profile of the furrow opening

4 Conclusions

Aiming at the problem that the discrete element simulation parameters of clay in the optimization study of furrow opener components for seeders in HAMA cannot accurately simulate the real operation of furrow opening, in this study, we adopted Bonding V2 and JKR V2 contact models to simulate clay in HAMA for the characteristics of clay and carried out the parameter calibration and validation. The specific conclusions are as follows:

(1) Combined with the measurements of intrinsic parameters of HAMA clay, we modeled HAMA clay particles with particle radii of 1, 3, and 5 mm. Compared with other studies, this model is the first to consider the effects of bonding and viscosity-wetness at the same time.

(2) The inter-particle contact adhesion characteristics of clay in HAMA were investigated by soil stacking angle test; static friction and rolling friction tests with 65Mn, the material of furrow opener parts, revealed the contact separation and friction characteristics of clay and 65Mn in HAMA.

(3) The tests simulated the mechanical behaviors such as shear deformation during the determination of clay compaction meter, and the normal/tangential stiffness per unit area had a large influence on the simulation results of compaction. The bonding parameters of the Bonding V2 contact model were calibrated by the PB, the steepest climb, and the BBD tests. The optimal combinations of significance parameters were 4.71×10^{7} N/m^{3} for normal stiffness per unit area, 2.32×10^{6} N/m^{3} for tangential stiffness per unit area, 23 080 Pa for critical tangential stress, and 2.75×10^{6} Pa for non-significance parameter.

(4) Straight-shear simulations and physical tests were used to investigate the Bonding V2 and JKR V2 contact model contact and bonding parameters for verification. The straight shear results show that the soil shear stress simulation value and the measured value of the trend are basically the same. The maximum shear stress has a relative error of 4.90%, which, compared with the existing model, is a further improvement of the simulation accuracy. The field test results of trenching operation further showed that the relative errors of the average value of trenching depth, qualification rate, and coefficient of variation of trenching operation indices were within 15%, indicating that the constructed contact models of Bonding V2 and JKR V2 of HAMA clays can provide a parameter basis for simulation and optimization of parameters of the trenching operation in HAMA.

This study can provide new ideas and explorations for the contact, adhesion, separation, and shear characteristics of clay and furrow opener component materials in HAMA, as well as for the study of deformation and motion laws during mechanized seeding using advanced computer simulation methods such as the discrete element method.

Acknowledgements

This study was supported by the National Key Research and Development Program of China (2021YFD2000404) and the Earmarked fund for CARS (CARS-08).

[References]

[1] Luo, X W. Thoughts on the development of agricultural mechanization in hilly and mountainous areas. Agric. Mach. Technol. Ext., 2011; 17–20.

[2] Wang X W, Yuan S Q, Jia W D. Current situation and development of agricultural mechanization in hilly and mountainous areas. Journal of Drainage and Irrigation Machinery Engineering (JDIME), 2022; 40(5): 535–540. (in Chinese).

[3] Zeng Z W, Ma X, Cao X L, Li Z H, Wang X C. Critical Review of Applications of Discrete Element Method in Agricultural Engineering. Transactions of the CSAM, 2021; 52(4): 1–20.

[4] Aikins K A, Ucgul M, Barr J B, Awuah E, Antille D L, Jensen T A, et al. Review of Discrete Element Method Simulations of Soil Tillage and Furrow Opening. Agriculture, 2023; 13: 541.

[5] Jasoliya D, Untaroiu A, Untaroiu C. A review of soil modeling for numerical simulations of soil-tire/agricultural tools interaction. J. Terramech., 2024; 111: 41–64.

[6] Mudarisov S, Farkhutdinov I, Khamaletdinov R, Khasanov E, Mukhametdinov A. Evaluation of the significance of the contact model particle parameters in the modelling of wet soils by the discrete element method. Soil Tillage Res., 2022; 215: 105228.

[7] Yang Q Z, Shi L, Shi A P, He M S, Zhao X Q, Zhang L, et al. Determination of key soil characteristic parameters using angle of repose and direct shear stress test. Int J Agric & Biol Eng, 2023; 16(3): 143–150.

[8] Yang L, Li J W, Lai Q H, Zhao L L, Li J J, Zeng R H, et al. Discrete element contact model and parameter calibration for clayey soil particles in the Southwest hill and mountain region. J Terramech, 2024; 111: 73–87.

[9] Aikins K A, Ucgul M, Barr J B, Jensen T A, Antille D L, Desbiolles J M A. Determination of discrete element model parameters for a cohesive soil and validation through narrow point opener performance analysis. Soil Tillage Res., 2021; 213: 105123.

[10] Zhou H, Che H L, Geng D Y, Chen M Z, Zhang Y P. Discrete element modeling and parameter calibration of typical soil in maize field tillage layer. Transactions of the CSAM, 2023; 54(11): 49–60, 113.

[11] Li J W, Tong J, Hu B, Wang H B, Mao C Y, Ma Y H. Calibration of parameters of interaction between clayey black soil with different moisture content and soil-engaging component in northeast China. Transactions of the CSAE, 2019; 35(6): 130–140. (in Chinese)

[12] Lu Q, Liu F J, Liu L J, Liu Z J, Liu Y Q. Establishment and verification of discrete element model for seed furrow soil-seed-covering device. Transactions of the CSAM, 2023; 54(10): 46–57.

[13] Sun J B, Liu Q, Yang F Z, Liu Z J, Wang Z. Calibration of discrete element simulation parameters of sloping soil on loess plateau and its interaction with rotary tillage components. Transactions of the CSAM, 2022; 53(1): 63–73.

[14] Yang Q Z, He M S, Shi L, Zhu M L, Li Z Y, He W B. Calibration of discrete element simulation parameters for interaction between layered cold soil and contact soil clearing tools. Journal of Jiangsu University(Natural Science Edition), 2023; 44(1): 52–61.

[15] Chen Z F, Duan A X, Liu Y, Zhao H Q, Dai C Y, Hu S, et al. Discrete element contact model and parameter calibration of sticky particles and agglomerates. J. Terramech., 2024; 116: 100998.

[16] Zhang Z H, Zhao L L, Lai Q H, Tong J. Operation mechanism analysis and experiments of shovel-type rolling soil-engaging components based on DEM-MBD coupling. Transactions of the CSAE, 2022; 38(15): 10–20. (in Chinese)

[17] Wang J W, Xu Y A, Wang C Y, Xiang Y S, Tang H. Design and simulation of a trenching device for rice straw burial and trenching based on MBD-DEM. Comput. Electron. Agric, 2023; 207: 107722.

[18] Wang D W, Lu T, Zhao Z, Shang S Q, Zheng S, Liu J. Calibration of discrete element simulation parameters for cultivated soil layer in coastal saline alkali soil. Transactions of the CSAM, 2024; 55(11): 240–249.

[19] Wang H C, Ding K Q, Xia J J, Zhang G Z, Wang Y, Kang Q X, et al. Calibration of disturbed-saturated paddy soil discrete element parameters based on slump test. Transactions of the CSAM, 2024; 55(S2): 222–230.

[20] Chen F, Yang L, Cui T, Zhang D X, He X T, Zhang K L, et al. Influence of the forward direction surface slope on the sowing depth operation performance of the mechanical profiling maize seeder. Soil Tillage Res., 2025; 252: 106600.

[21] Jia X, Zheng X P, Chen L C, Liu, C L, Song J N, Zhu C T, et al. Discrete element flexible modeling and experimental verification of rice blanket seedling root blanket. Comput. Electron. Agric., 2025; 233: 110155.

[22] Li S B, Huan X L, Wang T Y, Hui Y T, You Y, Wang D C. Biomechanical properties and discrete element modeling of PSR stalks during silage harvest. Comput. Electron. Agric, 2024; 217: 108644.

[23] Zhang F B, Luo Z T, Zheng E L, Han L, Qian J, Yao H P, et al. Imitating pangolin scale structure for reducing adhesion and resistance of rotary tillage in wet-adhesive soil. Soil Tillage Res., 2025; 245: 106306.

[24] Wang X Z, Zhang S, Pan H B, Zheng Z Q, Huang Y X, Zhu R X. Effect of soil particle size on soil-subsoiler interactions using the discrete element method simulations. Biosystems Engineering, 2019; 182: 138–150.

[25] He D, Li H W, He J, Lu C Y, Wang C, Wang Y B, et al. Research on vibration characteristics of no-tillage seeding unit based on the MBD-DEM coupling. Comput. Electron. Agric., 2025; 230: 109877.

[26] Li H, He J, Wang Q J, Wang C, Wu Z Y, Guo Z Y. Analysis of slope-adaptive in covering-compacting device for no-till sowing based on DEM-MBD. Comput. Electron. Agric., 2025; 233: 110175.

[27] Sun K, He C L, Zhou Q, Yu X N, Dong Q, Wang W J, et al. Study on the influence mechanism of soil covering and compaction process on maize sowing uniformity based on DEM–MBD coupling. Agronomy, 2024; 14: 2883.

[28] Xie D B, He J X, Liu T, Liu C, Zhao G, Chen L Q. Establishment and validation the DEM-MBD coupling model of flexible straw-Shajiang black soil-walking mechanism interactions. Comput. Electron. Agric., 2024; 224: 109203.

[29] Zou L L, Yan D W, Niu Z R, Yuan J, Cheng H, Zheng H. Parametric analysis and numerical optimisation of spinach root vibration shovel cutting using discrete element method. Comput. Electron. Agric., 2023; 212: 108138.

[30] Zhang S L, Zhao H B, Wang X Z, Dong J X, Zhao P F, Yang F F, et al. Discrete element modeling and shear properties of the maize stubble-soil complex. Comput. Electron. Agric., 2023; 204: 107519.

[31] Song Z H, Li H, Yan Y F, Tian F Y, Li Y D, Li F D. Calibration method of contact characteristic parameters of soil in mulberry field based on unequal-diameter particles DEM theory. Transactions of the CSAM, 2022; 53(6): 21–33.

[32] Potyondy D O, Cundall P A. A bonded-particle model for rock. International Journal of Rock Mechanics and Mining Sciences, 2004; 41(8): 1329–1364.

[33] Thornton C. Granular dynamics, contact mechanics and particle system simulations: A DEM study, particle technology series. Springer International Publishing, Cham, 2015 https://doi.org/10.1007/978-3-319-18711-2

[34] Xiong P Y, Yang Z, Sun Z Q, Zhang Q Q, Huang Y Q, Zhang Z W. Simulation analysis and experiment for three-axis working resistances of rotary blade based on discrete element method. Transactions of the CSAE, 2018; 34(18): 113–121. (in Chinese)

[35] Wu A X, Sun Y Z, Liu X P. Granular dynamics theory and its applications, 2002. Metallurgical industry press.

[36] Beakawi Al-Hashemi H M, Baghabra Al-Amoudi O S. A review on the angle of repose of granular materials. Powder Technology, 2018; 330: 397–417.

[37] Jia H L, Wang W P, Chen Z, Zheng T Z, Zhang P, Zhuang J. Research status and prospect of soil-engaging components optimization for agricultural machinery. Transactions of the CSAM, 2017; 48(7): 1–13.

[38] Barr J B, Ucgul M, Desbiolles J M A, Fielke J M. Simulating the effect of rake angle on narrow opener performance with the discrete element method. Biosystems Engineering, 2018; 171: 1–15.